

Meso-scale size effects of material heterogeneities on crack propagation in brittle solids

Liuchi Li^{a,*}, Jack Rao^b, Todd C. Hufnagel^{a,b,c}, K.T. Ramesh^{a,b,c}

^a*Hopkins Extreme Materials Institute, Johns Hopkins University, Baltimore, MD 21218, USA*

^b*Department of Mechanical Engineering, Johns Hopkins University, Baltimore, MD 21218, USA*

^c*Department of Materials Science and Engineering, Johns Hopkins University, Baltimore, MD 21218, USA*

Abstract

Brittle solids are often toughened by adding a second-phase material. This practice often results in composites with material heterogeneities on the meso scale: large compared to the scale of the process zone but small compared to that of the application. The specific configuration (both geometrical and mechanical) of this mesoscale heterogeneity is generally recognized as important in determining crack propagation and, subsequently, the (effective) toughness of the composite. Here, we systematically investigate how dynamic crack propagation is affected by mesoscale heterogeneities taking the form of an array of inclusions. Using a variational phase-field approach, we compute the apparent crack speed and fracture energy dissipation rate to compare crack propagation under Mode-I loading across different configurations of these inclusions. If fixing the volume fraction of inclusions, matching the inclusion size to the K-dominance zone size gives rise to the best toughening outcome. Conversely, if varying the volume fraction of inclusions, a lower volume fraction configuration can lead to a better toughening outcome if and only if the inclusion size approaches from above the size of the K-dominance zone. Since the size of the K-dominance zone can be estimated *a priori* given an understanding of the application scenario and material availability, we can, in principle, exploit this estimation to design a material's mesoscale heterogeneity that optimally balances the tradeoff between strength and toughness. This paves the way for realizing functional (meta-)materials against crack propagation in extreme environments.

Keywords: Dynamic fracture, Crack speed, Fracture energy, K-dominance zone, Inclusion configuration

1. Introduction

Structural materials such as glass and ceramics find applications across multiple industrial sectors, from aerospace to defense, where extreme environments (such as high-speed impact) are often encountered. However, these strong and lightweight materials are often brittle, and this creates significant concerns regarding product reliability in safety-critical applications. Thus, it has been a common practice to toughen a brittle material by adding a second material phase to

*Corresponding author

Email address: 11i128@jhu.edu (Liuchi Li)

alter the fracture behavior. Such approaches often result in mesoscale material heterogeneities: the heterogeneity length scale is large compared to that of the process zone, but small compared to that of the application (which gives rise to “extrinsic toughening mechanisms” [1, 2]). As such, this practice enjoys a very high-dimensional design space in terms of not only what material to choose as the second phase but also how to configure this second phase spatially with respect to the base material phase, given the significant separation of length scales.

The biggest challenge, therefore, lies in how we effectively explore this design space (in terms of choosing materials and their geometrical configurations) to minimize the well-known tradeoff between strength and toughness [1, 3]. For instance, adding a more compliant or tougher phase can help arrest a propagating crack, thereby toughening the material. However, such inclusions can also lead to a decrease in the overall stiffness and strength. Historically, this design space has been explored by focusing on the choice of the second phase material. Examples include crystallized ceramic inclusions in an LS_2 glass matrix [4] and TiC particles in a SiC ceramic matrix [5]. The issue is that, partly due to synthesis and processing limitations, the resulting geometrical configuration of the material heterogeneity is usually stochastic and not well-controlled, leaving the geometrical aspect (a considerable portion of this design space) largely unexplored.

Recently, advances in manufacturing techniques allow the precise control of a material’s structure across scales, making it possible to systematically explore the geometric aspect of this design space. There are particularly promising opportunities within the context of mechanical “meta-materials”¹ which have already demonstrated novel mechanical properties (such as a high stiffness-to-density ratio [6, 7], with chiral character [8], and being (re-)programmable [9, 10, 11]) that are not found in conventionally manufactured materials. [12, 13] provide comprehensive introductions to this topic. An emergent research area is that of studying the fracture resistance of these meta-materials [14, 15, 16, 17, 18], particularly the class of meta-materials containing arrays of compliant inclusions (which often take the form of voids [19, 20, 21]). These studies recognized that the geometrical configuration of these inclusions (mainly size and spacing) could alter crack propagation behaviors [2, 19]. It has been argued that the size of the K -dominance zone plays an important role in this regard [2]. A properly designed configuration can thus lead to attaining high toughness [21, 22], and even directional asymmetry toughness when designing inclusion shape comes into play as well [23].

However, a systematic and quantitative understanding is still lacking with regard to the mesoscale size effects of material heterogeneities on dynamic fracture. Many important questions remain unanswered, especially from a physics-guided design perspective. For instance, why should we choose a specific inclusion size over another? Does changing the inclusion size necessitate a change of inclusion spacing to maintain a “sweet spot” design? Lastly, how important are the material properties of the inclusions? These questions are also relevant for minimizing the undesired effects of these inclusions (for instance, those in the form of voids) on the overall material stiffness and strength, which are especially important for applications in extreme environments.

Here, we systematically quantify the mesoscale size effects of material heterogeneities on fracture propagation in a brittle composite (or meta-) material. Recognizing that fracture

¹The terms “metamaterials” and “architected materials” are often used interchangeably in the literature.

propagation in a medium with mesoscale heterogeneities can give rise to considerable inertia effects [24, 25, 26, 27], we use a dynamic phase-field approach [28] for numerical simulation. This approach enables us to calculate fracture energy dissipation rate and crack speed at every instant. Similar to previous studies [2, 29], we consider (tougher) inclusions as mesoscale material heterogeneities, and we model them and the base medium as separate continuum solids that homogenize out any possible micro-scale (and below) material heterogeneities. Beyond what has been done in prior studies [21, 23], we consider the configuration of these inclusions under both varying and fixed volume fraction settings and different constituent materials. By doing so, we can cover a larger fraction of the design space. We are particularly interested in the possibility of a low-volume fraction design outperforming a high-volume fraction design in toughening a composite material (i.e., lower crack speed and higher fracture energy dissipation rate). The underlying physical interpretations can have practical implications in designing functional materials that optimally balance the tradeoff between strength and toughness [1] (and potentially simultaneously realize low mass densities [14]).

The rest of this paper is organized as follows. In section. 2, we briefly introduce the variational phase-field approach for dynamic fracture simulation; In section. 3, we discuss our numerical model and analysis procedure. In section. 4, we discuss simulation results that demonstrate the relative size interplay between the inclusion and the K-dominance zone. In section. 5, we present a summary and discuss future directions.

2. Variational phase-field approach to fracture

Phase-field modeling provides a mathematical framework that is widely used to describe physical systems, especially those with evolving interfaces far from equilibrium (fracture propagation in solids is a typical example). Since its first introduction in the context of solidification and phase transition [30], it has been adapted to modeling many other phenomena such as multiphase flow [31, 32], collection cell dynamics [33, 34], and material failures [35, 36, 37], to name a few. At the core of phase-field modeling is a mathematical description of a physical system's energy (density) γ_ℓ , a quantity associated with the particular physical field of modeling interest. This is done using a scalar field $\phi \in [0, 1]$ that varies smoothly in space over a length scale parameter ℓ . In the particular case of fracture, we can view γ_ℓ as a (regularized) fracture energy density over the entire simulation domain, with the length scale ℓ being used to effectively smear out the crack, so that $\phi = 0$ typically indicates intact material and $\phi = 1$ indicates completely damaged material. It has been shown that ℓ determines the threshold for crack nucleation [38], and from a physics standpoint, it can be viewed as a representation of active mechanisms in the process zone [39]. When modeling dynamic fracture problems, we seek to minimize an incremental Lagrange energy functional \mathbf{I}_ℓ using the principle of least action (see [40, 28] for a comprehensive discussion relevant to the topic). The functional form is:

$$\mathbf{I}_\ell(u, \dot{u}, \phi) = \int_{t_1}^{t_2} \left\{ \int_{\Omega} \left[\frac{\rho}{2} |\dot{u}|^2 - \mathcal{W}^e(u, \phi) - G_C \gamma_\ell(\phi, \nabla \phi) + \rho b \cdot u \right] d\Omega + \int_{\partial\Omega} \mathbf{t} \cdot u dS \right\} dt, \quad (2.1)$$

under the constraint $\dot{\phi} > 0$, to account for the irreversibility of the fracture process. In Eqn. 2.1, u is the displacement field, with $\dot{u} = \frac{\partial u}{\partial t}$ the velocity field, ρ the material density, ϕ the phase

field parameter indicating the degree of material damage, \mathcal{W}^e the elastic strain energy density, G_C the critical energy release rate (or fracture toughness) [41], γ_ℓ the (regularized) fracture energy density, b the gravitational constant, and \mathbf{t} the surface traction. The form (or degree of complexity) of \mathcal{W}^e , Γ_ℓ , and G_C may be problem-specific (e.g., G_C may be anisotropic [42] and γ_ℓ may be dependent on higher-order terms of ϕ [43]) and even Eqn. 2.1 can be modified to model ductile instead of brittle fracture [44, 45, 46]. In this work, we restrict ourselves to materials that are isotropic and linear elastic, with rate-independent fracture toughness. We can describe a material by three parameters: Young’s modulus E , Poisson’s ratio ν , and fracture toughness G_C . Interfacial effects [47] can be included by incorporating a cohesive zone model [48], but we neglect them for the purposes of this work, leaving that to a subsequent effort. We adopt the following form of γ_ℓ , commonly used for modeling brittle fracture [40]:

$$\gamma_\ell = \frac{1}{4c_w\ell} (w(\phi) + \ell^2|\nabla\phi|^2), \text{ with } c_w = \frac{1}{2} \text{ which implies } w(\phi) = \phi^2. \quad (2.2)$$

We implement this method using FEM in 2D based on our previous work on modeling multi-body contact mechanics problems [49]. The source code is publicly available at <https://github.com/liuchili/Variational-phase-field-method-for-dynamic-fracture-problem.git>.

Our implementation finds the stationary solution to Eqn. 2.1 in parallel based on the alternating minimization scheme, utilizing an in-house conjugate gradient solver that runs with OpenMP and MPI. In particular, we use the average acceleration scheme to solve for u . At each time step, we iterate back and forth between u and ϕ until convergence is achieved. We verified our implementation using the classical Kalthoff-Winkler experiment [50] (see Appendix for details).

3. Modeling fracture propagation in brittle solids with mesoscale heterogeneities

We use the variational phase-field method discussed above to simulate dynamic crack propagation under Mode-I crack opening mode in the plane-stress condition, using a single-notched three-point bending configuration (with span L , height H , and notch length a) that is subjected to a constant indentation velocity v_{load} as shown in Fig. 1(a). We consider a simple case where we represent mesoscale material heterogeneities as square-shaped inclusions. We arrange these inclusions (with a uniform size d) as a single array (with a uniform spacing h) along a line aligned with the expected crack propagation path, starting from a distance of D_{in} from the notch tip (a “buffer zone”) and extending to a length of L_{in} , as shown in Fig. 1(b). Next, we introduce a design parameter, the number of inclusions, N , to determine h and d , considering both varying and fixed volume fraction scenarios. We begin with the scenario of varying volume fraction $f_1 = \frac{Nd^2}{WL_{\text{in}}}$ where we pick $W = 10L_{\text{in}}$ (see Fig. 1(b)), which is large enough such that (1) the crack can only interact with a single array of inclusions, and (2) the stress fields developed from any two neighboring inclusion arrays (with a separation distance of $W = 10L_{\text{in}}$) do not interact². Because of this, we only consider a single array of inclusions right above the notch to reduce simulation expenses. Plugging in $W = 10L_{\text{in}}$, we have $f_1 = \frac{Nd^2}{10L_{\text{in}}^2}$. We further enforce the following two conditions:

²Note that this can be a conservative estimation.

$$\frac{Nd}{L_{\text{in}}} = c \text{ and } Nh = L_{\text{in}}, \text{ with } c = \frac{d}{h} \in [0, 1] \text{ being a user-defined constant.} \quad (3.1)$$

For a given value for c (we fix $c = 0.2$ throughout this work), varying N provides different geometrical configurations represented by different (d, h) combinations. Keeping c unchanged allows us to isolate the effect of inclusion size from spacing for different configurations. This design strategy enables varying inclusion size and volume fraction at the same time, with the volume fraction $f_1 = \frac{c^2}{10N}$, so $f_1 \propto N^{-1}$ shown as the blue curve in Fig. 1(c). We also have $d \propto N^{-1}$ following this condition. Fig. 1(d) shows three different combinations of (d, h) using this design strategy with $N = 3$, $N = 5$, and $N = 15$, respectively. Next, we consider the scenario of fixed volume fraction (denoted as f_2), which we choose to be equal to f_1 under the configuration shown with $N = 5$, so $f_2 = \frac{c^2}{50}$ represented as the green curve in Fig. 1(c). This allows us to again find different (h, d) combinations by varying N . A simple calculation gives the following relation between (d, h) and N for $f_2 = \frac{c^2}{50}$:

$$d = \frac{cL_{\text{in}}}{\sqrt{5N}}, \text{ and } h = \frac{L_{\text{in}}}{\sqrt{5N}}. \quad (3.2)$$

We omit examples for this scenario, but all resulting configurations follow the spacing pattern shown in Fig. 1(b). Lastly, in this work, we choose $L = 32a$, $H = 8a$, $L_{\text{in}} = 5a$, and $D_{\text{in}} = a$, where a is the initial crack length (notch length).

In addition to the geometrical configurations, we also vary the mechanical configurations by selecting different values for α (representing the elastic contrast) and β (representing the toughness contrast):

$$\alpha = E_{\text{in}}/E_0, \text{ and } \beta = G_{\text{C, in}}/G_0, \quad (3.3)$$

where E_{in} ($G_{\text{C, in}}$) is Young's modulus (toughness) of the inclusion material, with E_0 ($G_{\text{C, 0}}$) being that of the base material. In this work, we choose inclusions made from tougher materials with $\beta \in [1.2, 2.4]$, and consider a range of stiffness contrast $\alpha \in [0.2, 1.2]$. We pick glass (a typical brittle material) to be our base material, with E_0 and $G_{\text{C, 0}}$ values reported in [4], which gives a length scale $\ell \simeq 0.02a$ [51].

For simplicity, we consider dynamic fracture under a quasi-static loading condition in this work. Note that a quasi-static loading condition means wave propagation associated with the external load happens sufficiently fast; However, this does not imply the material response is quasi-static in the presence of fracture³. Brittle fracture can be fast and can cause considerable material inertia effects [52]. As such, we use a dynamic phase-field formulation to explicitly account for crack speed and any inertia effects associated with a fast-propagating crack tip. To achieve a quasi-static loading condition while maintaining computational feasibility, we use a loading velocity $v_{\text{load}} \sim 5 \times 10^{-5}v_R$ for all simulations where v_R is the Rayleigh wave speed

³In contrast, dynamic loadings will induce inertia effects in the form of propagating mechanical disturbances that strike a crack and cause fracture propagation. Spall is a typical example in this regard.

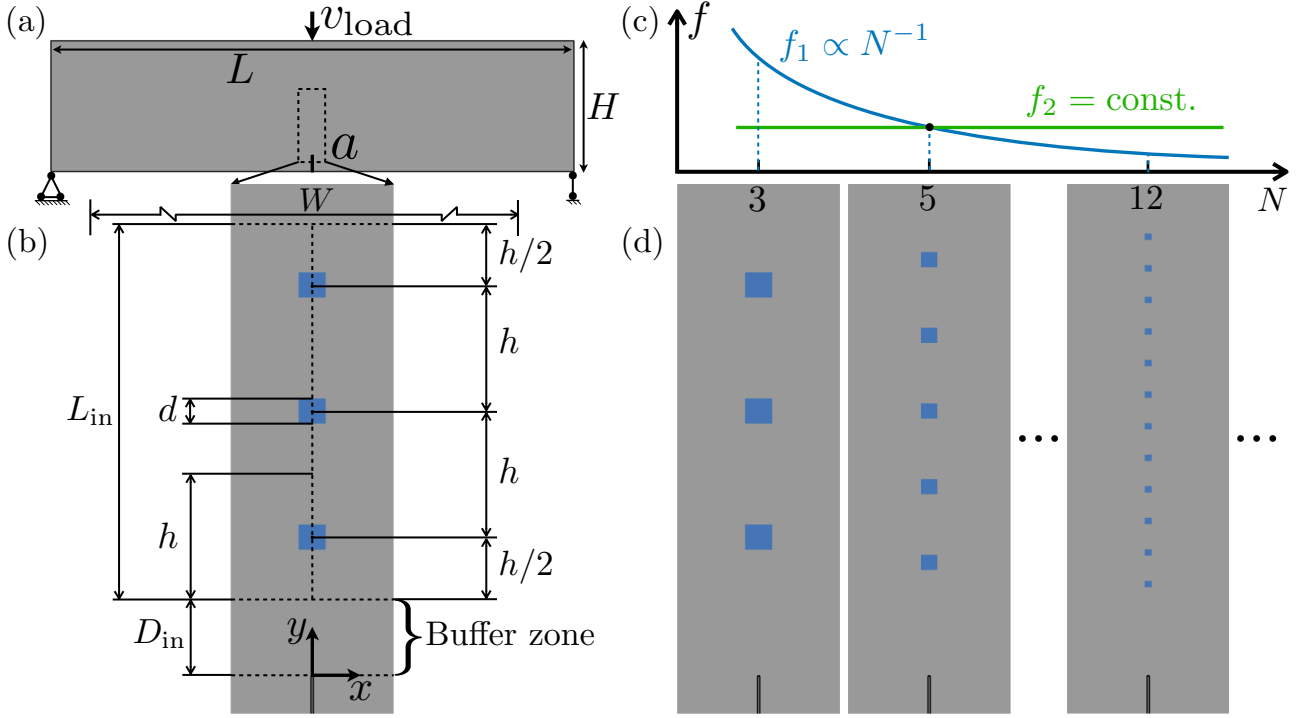


Figure 1: (a) The setup of our numerical model: a single-notched three-point bending beam subjected to a constant indentation speed v_{load} . The beam has a span L , a height H , and a notch with length a . (b) The geometrical configuration of a single array of mono-sized (d) and equally-spaced (h) inclusions embedded along a line with length L_{in} which starts at a distance of D_{in} (as a buffer zone) from the notch tip. The width $W = 10L_{\text{in}}$ considered for computing volume fraction is not drawn to scale. In this particular image, we have the inclusion number $N = 3$. Varying this value will lead to a different geometrical configuration. (c) Variation of the volume fraction of inclusions as a function of N . We consider two scenarios: a varying volume fraction scenario where $f \propto N^{-1}$ (blue curve) and a fixing volume fraction scenario where $f_2 = f_1$ (green curve) using f_1 determined from $N = 5$. (d) Visualization of the geometrical configuration of inclusions under the varying volume fraction scenario with $N = 3$, $N = 5$, and $N = 12$.

of the glass. (It is generally recommended $v_{\text{load}} < 1\%v_R$ [53] to ensure a quasi-static loading condition.) We run all simulations for the same amount of time t over irregular linear triangular elements that are locally refined within the crack propagation region. Elements within this region all have size $\delta \simeq \ell/3$, which is small enough to resolve crack evolution with sufficient accuracy [54]. We note that ℓ imposes a length scale on material heterogeneity, below which a crack tip always senses a homogeneous field [2]. As such, for all configurations, we make sure the inclusion size d is strictly larger than ℓ . We also note that this finite-element discretization results in a numerical fracture toughness G_C^{num} whose value is different than the theoretical one G_C [36]:

$$G_C^{\text{num}} = G_C \left(1 + \frac{\delta}{c_w \ell}\right), \quad (3.4)$$

where c_w is the normalization constant presented in Eqn. 2.2. As such, we use G_C^{num} when applying fracture mechanics theories to analyze simulation results. On average, every simulation takes about 8 hours to finish on the Rockfish high-performance computing facility at Hopkins,

using 16 MPI tasks with six threads per task. We confirm that for all configurations considered in this work, we observe negligible differences in the crack initiation time and propagation within the buffer zone (whose length is D_{in}). This observation makes it straightforward to ensure that our subsequent analysis isolates the effect of material heterogeneity on dynamic crack propagation.

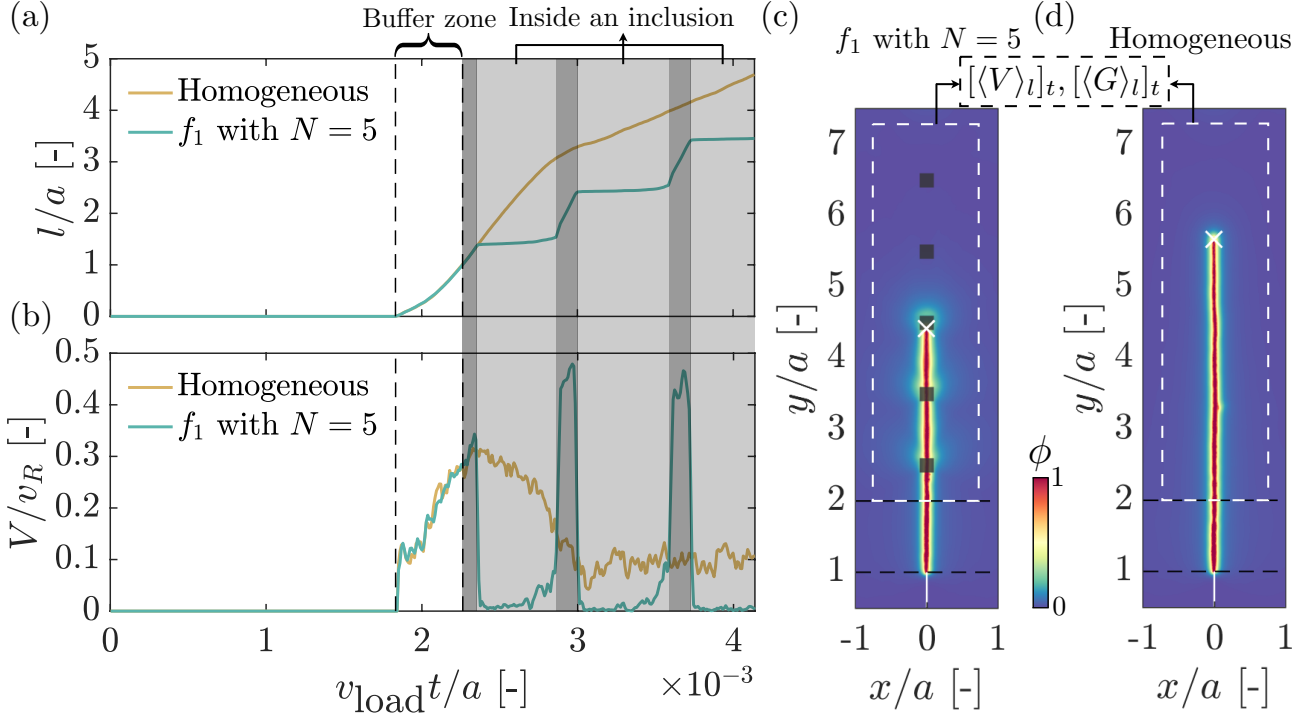


Figure 2: (a) Evolution of normalized crack length l/a as a function of normalized indentation displacement $v_{\text{load}} t/a$ for a homogeneous case with no inclusion (yellow curve) and a heterogeneous case with five inclusions (blue curve). The inclusion material has an elastic contrast $\alpha = 0.4$ and a toughness contrast $\beta = 2.4$. The two alternating shaded areas indicate two different kinds of crack tip locations for the heterogeneous case. The area colored in dark grey indicates the crack tip being outside an inclusion and otherwise inside an inclusion. The (almost) constant crack length within each light grey area indicates the crack is arrested inside the inclusions. (b) A plot similar to (a) shows the variation of normalized instantaneous crack tip speed V/v_R , where v_R is the Rayleigh wave speed of the base material. (c) A visualization of the final crack trajectory based on ϕ showing the interaction between the crack and the inclusions for the heterogeneous case. The white cross indicates the identified crack tip, and the white dashed rectangle indicates the region within which $[\langle V \rangle]_t$ and $[\langle G \rangle]_t$ are calculated. (d) A similar visualization to (c) shows the result from the homogeneous case.

As a representative result, Fig. 2(a) shows the evolution of normalized crack length (l/a) as a function of normalized indentation displacement ($v_{\text{load}} t/a$), where we calculate l by tracking the crack tip spatially temporally based on the phase field ϕ (locating the tip of an iso-curve with a threshold value $\phi = 0.85^4$, see Appendix for details). Two configurations are included in this figure: a homogeneous one with no inclusions (yellow curve) and a heterogeneous one with five inclusions (green curve, material properties are $\alpha = 0.4, \beta = 2.4$). The crack growth begins

⁴We have tried varying this threshold value ranging from 0.75 to 0.95, from which the resulting crack tip locations show negligible differences.

simultaneously in both cases, and the evolution of crack length remains identical until leaving the buffer zone. This observation is demonstrated through the corresponding (normalized) instantaneous crack tip speed (V/v_R with V being calculated using l and t), as shown in Fig. 2(b). After a crack leaves the buffer zone, it enters the region where inclusions may reside. The shaded area in Fig. 2(a)(b) with two alternating colors indicates two different regions for crack propagation in the heterogeneous configuration: light grey indicates the region where the crack propagates inside inclusions while dark grey indicates otherwise. We observe that the crack gets (almost) arrested inside inclusions: l is (almost) constant, and V is (almost) zero. Figs. 2(c) and 2(d) visualize the final crack patterns for these two configurations, where the white cross marker in each image indicates the identified crack tip location. This observation of the crack propagating through inclusions with fluctuating speed is consistent with experimental studies [25]. We emphasize that the specific crack propagation pattern is size-dependent and material-dependent. In other words, by changing the choice of inclusion size and material, a crack may not propagate through inclusions.

Our main interest is thus to quantify and compare different crack propagation patterns resulting from different inclusion sizes and material choices. We do so using two temporally averaged variables: the apparent crack speed $[\langle V \rangle_l]_t$ and the apparent fracture energy dissipation rate $[\langle G \rangle_l]_t$. Here, $\langle \cdot \rangle_l$ denotes the average of a quantity at a given time instant over the crack length l , and $[\cdot]_t$ denotes the arithmetic average of a quantity over every time instant t . We do not calculate V and G until a crack leaves the buffer zone. As an example, the two dashed black rectangles shown in Figs. 2(c) and 2(d) indicate the regions within which V and G are calculated.

As to our calculation procedure. First, at every instant t_i , we can calculate the crack length l_i (by tracking the crack tip location), and we can also calculate the fracture energy $\Gamma_\ell^i = \int_\Omega \gamma_\ell^i d\Omega$, where γ_ℓ^i is the (regularized) fracture energy density (as a function of ϕ) at t_i . This allows us to compute $\langle V \rangle_{l_i} = l_i/t_i$ and $\langle G \rangle_{l_i} = \Gamma_\ell^i/l_i$. Above, $i \in [1, N_t]$ with N_t being the number of time instants sampled from each simulation. Then, we perform an arithmetic average over t_i to get $[\langle V \rangle_l]_t = \frac{1}{N_t} \sum_{i=1}^{N_t} \langle V \rangle_{l_i}$ and $[\langle G \rangle_l]_t = \frac{1}{N_t} \sum_{i=1}^{N_t} \langle G \rangle_{l_i}$. Lastly, for simplicity, we use the following two non-dimensionalized parameters for comparing $[\langle V \rangle_l]_t$ and $[\langle G \rangle_l]_t$ across different configurations:

$$\tilde{V} = \frac{[\langle V \rangle_l]_t}{[\langle V_0 \rangle_l]_t}, \text{ and } \tilde{G} = \frac{[\langle G \rangle_l]_t}{[\langle G_0 \rangle_l]_t}, \quad (3.5)$$

where V_0 and G_0 follow the same definition of V and G , but they are computed from the homogeneous configuration. Self-evidently, a smaller value of \tilde{V} and a larger value of \tilde{G} indicate a better toughening outcome than that from the homogeneous configuration: lower crack speed and higher fracture energy dissipation rate. We report and discuss our results in the following sections.

4. Results and discussion

4.1. Identical volume fraction with fixed inclusion material

We discuss results obtained from configurations with identical volume fraction $f_2 = f_1|_{N=5}$. The resulting inclusion size ranges from $\sim 0.06a$ to $\sim 0.26a$. We fix the choice of inclusion

material to be $\alpha = 0.4, \beta = 2.4$, so more compliant and tougher inclusions. Fig. 3(a) shows the variation of \tilde{V} (data in blue) and \tilde{G} (data in red) as a function of d , where we normalize d using d_{\max} (obtained from the configuration with $N = 3$). Qualitatively, varying d monotonically leads to non-monotonic variations of \tilde{V} and \tilde{G} . When d is on the larger side (larger than $0.4d_{\max}$ residing within the green region), decreasing the inclusion size d leads to better toughening outcomes: \tilde{V} (slowly) decreases and \tilde{G} increases. However, the trend is reversed as d keeps decreasing to be smaller (smaller than $0.4d_{\max}$ residing within the orange region). Subsequently, a transition point arises corresponding to the most ideal toughening outcome. Since the exact transition location is unclear, we overlap the green and orange regions qualitatively, as shown in Fig. 3(a). We can also observe a similar kind of transition in terms of crack trajectory. Fig. 3(b) shows the final crack trajectory for five different configurations highlighted in Fig. 3(a). When d is on the larger side (configurations one and two residing in the green region), the crack always goes through inclusions. However, the crack starts deflecting away as d keeps decreasing to be smaller (configurations three to five transitioning into the orange region). A crack deflecting away means fewer interactions with (tougher and more compliant) inclusions, which may be understood as the cause for increasing \tilde{V} and decreasing \tilde{G} in the orange region.

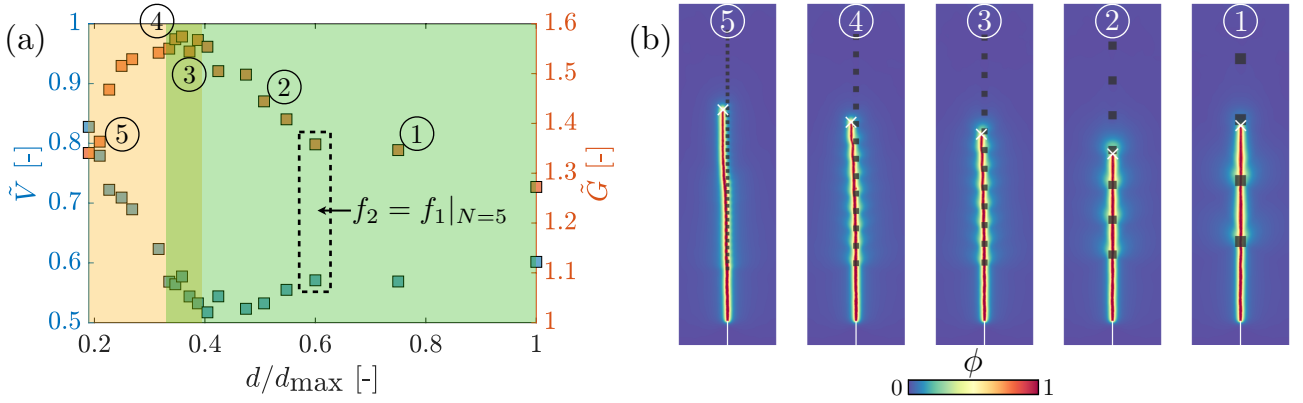


Figure 3: Scenarios with identical volume fractions. (a) Variation of \tilde{V} (blue square) and \tilde{G} (red square) as a function of normalized inclusion size d/d_{\max} , where d_{\max} corresponds to d determined from $N = 3$. The two data points encompassed by the black dashed rectangle are from the configuration with $f_1|_{N=5}$. Five configurations are highlighted. (b) Visualizations of the final crack trajectory for the five configurations are highlighted in (a). Again, the white cross in each image indicates the identified crack tip.

So, from Figs. 3(a) and 3(b), the size of inclusion d has an effect on crack propagation, and it governs the transition of the crack-inclusion interaction as well as that of the variation of \tilde{V} and \tilde{G} . We argue that this kind of size effect can be quantitatively explained by an interplay between the size of inclusion and that of the K-dominance zone (denoted as D_K) associated with the inclusion material. The foundation of our argument is the fact that at least for brittle materials that satisfy the *small-scale yielding* condition [39], a crack evolves by sensing and exploring the stress field inside the K-dominance zone [55, 23], an annulus that sits in between the much-smaller-sized process zone (where inelastic processes prevail) and the boundary condition-dependent zone (where boundary effects prevail), as shown in Fig. 4(a). More specifically, although where a crack decides to evolve depends on the *local* location

(on the scale of the process zone) at which stress satisfies $\sigma = \sigma_Y$, where precisely this *local* location is depends *non-locally* on a surrounding area (i.e., on the scale of the K-dominance zone where $\sigma \propto K_{IC}/\sqrt{r}$ [55]). Above, σ_Y is the material's yield strength, and $\sigma \propto K_{IC}/\sqrt{r}$ is the leading-effect term of the solution from Linear Elastic Fracture Mechanics (LEFM) theory. In this expression, K_{IC} is the critical Mode-I stress intensity factor (a material property given by $K_{IC} = \sqrt{GE}$ in plane-stress condition), and r is the distance to the crack tip.

Consequently, when a crack faces an inclusion and needs to decide how to proceed, the size of that inclusion with respect to that of the K-dominance zone becomes relevant. Suppose the inclusion is large enough to encapsulate the K-dominance zone (such that the location of σ_Y can be determined using solely the inclusion material $K_{IC, in} = \sqrt{\alpha\beta}K_{IC,0}$), the crack tip senses a homogeneous material field (corresponding to the inclusion material). When the inclusion size is not large enough to encapsulate the K-dominance zone (but still large enough to be qualified on the mesoscopic scale), the crack tip senses a heterogeneous material field: part of this field consists of the inclusion and part of this field consists of the base medium. This leads to a stress modulation within the K-dominance zone, which may change the location where $\sigma = \sigma_Y$, and may subsequently cause crack deflection depending on the particular choice of α and β . So in principle, if we have a sense of the size of the K-dominance zone associated with the inclusion material, we should be able to identify more quantitatively the transition location observed qualitatively from Figs. 3(a).

Estimating the size of the K-dominance zone is a complex and challenging process. From a theoretical point of view, the size of the K-dominance zone depends on both the length scale of the crack and that of the application (e.g., size and geometry). Ideally, for a stationary crack propagating in a large enough homogeneous medium, the size of the K-dominance zone will not change; however, this is no longer true when a crack evolves to be close enough to the application boundary. Further, non-uniform crack tip motion (commonly occurs when crossing heterogeneity boundaries) can play a role. It is well understood that it alters the quasi-static solution by scaling through the instantaneous crack tip speed [24]. Here, we use some simplifications to estimate D_K as a first-order approximation. First, we assume negligible changes in the K-dominance zone size for our configurations. Accordingly, we estimate D_K when a crack initiates from the notch tip. Second, we neglect the crack speed effect on the K-dominance solution, meaning the quasi-static formulation is adopted. Finally, following this quasi-static approximation, we normalize the inclusion material property to be $E_{in} = E_0, G_{C, in} = \alpha\beta G_{C0}$ to estimate the size of the K-dominance zone. We will also use this normalization to study other inclusion materials with different α but identical $\alpha\beta$ (i.e., identical $K_{IC, in}$). We discuss relevant results in Section. 4.3. Fig. 4(b) shows the spatial distribution of $(\sigma_{xx} + \sigma_{yy})/E_0$ at the moment of crack initiation, under the same loading condition for a homogeneous configuration with $E = E_0, G_C = 0.96G_{C0}$ (since $0.4 \times 2.4 = 0.96$). The black cross in Fig. 4(b) represents the crack tip identified based on the value of the phase field ϕ . We extract stress along the crack propagation direction and denote the distance to the crack tip as r .

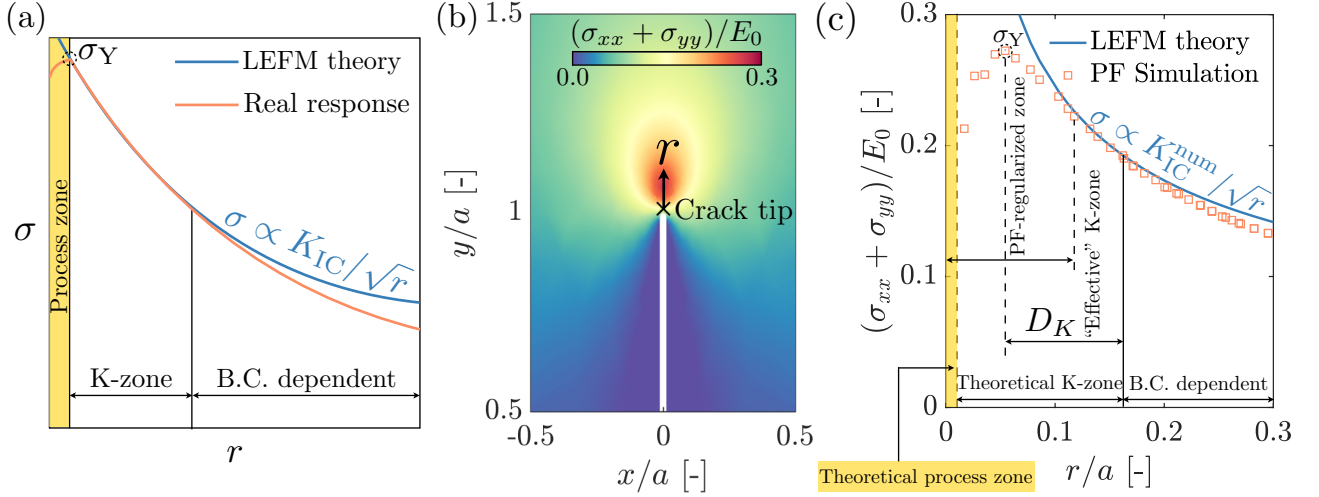


Figure 4: (a) A schematic showing the variation of stress σ as a function of the distance r to the crack tip, based on either the LEFM theory (blue curve) or the real response of a brittle material (red curve). Three regions can be identified. Very close to the crack tip is the process zone (colored in yellow), where inelastic material responses prevail, and LEFM theory breaks down. Ahead of the process zone is an annulus called the K-dominance zone, where LEFM theory holds. At the junction of these two zones, the material achieves its yield strength σ_Y . After the K-dominance zone, boundary effects prevail, and LEFM theory breaks down again. (b) A visualization showing the spatial distribution of $(\sigma_{xx} + \sigma_{yy})/E_0$ at the moment of crack initiation for a homogeneous material with $E = E_0$ and $G_C = 0.96G_{C0}$. Using the black cross, we indicate the crack tip location and denote the vertical distance away from the crack tip as r . (c) Variation of $(\sigma_{xx} + \sigma_{yy})/E_0$ as a function of the normalized distance r/a extracted from (d). The red squares are from a phase-field simulation, and the blue curve corresponds to the prediction obtained from LEFM theory. The “effective” K-dominance zone has a size D_K , which starts from where the stress peaks to where the stress deviates from the LEFM prediction. The PF-regularized zone is where the stress deviates from the LEFM prediction as approaching the crack tip due to a regularization imposed via ℓ (and finite element discretization). The theoretical process zone as well as the K-dominance zone, both discussed in (a), are also shown.

To estimate D_K , we overlay the extracted stress distribution with that calculated from the quasi-static near-tip field solution $\sigma_{xx} + \sigma_{yy} = 2K_{IC}/\sqrt{2\pi r} + \text{H.O.T.}$, in a way similar to [56]. We emphasize that this estimation should be done in a way that makes sense in the context of (phase-field) finite-element simulations. Consequently, this will give a D_K value that differs from the theoretical one, as shown qualitatively in Fig. 4(c) and in comparison with Fig. 4(a). There are two reasons behind this difference. First, finite-element discretization introduces an approximation that becomes especially pronounced near the crack tip, i.e., how well a simulation resolves the elasticity depends on the fineness of the mesh near the crack tip. This can lead to a larger deviation from the theoretical prediction of elasticity as we move closer to the crack tip. Second, phase-field regularization introduces an additional approximation to the (theoretically) sharp crack tip. This regularization will lead to a stress drop, as shown in Fig. 4(c) as we approach the numerically-identified crack tip (i.e., $\phi \rightarrow 1$). Such a stress drop may be interpreted to account for mechanisms active inside the process zone, which is missing from the elastic model considered in our simulations. From a different perspective, as $\ell \rightarrow 0$, the material yield strength goes to infinity, consistent with LEFM theory and Γ -convergence arguments [51]. The pattern of stress drop depends on the specific model used to express the fracture energy density term shown in Eqn. 2.2. For instance, we use the so-called AT2

model ($c_w = 1/2$) [51] in this work, which is known to behave differently than the AT1 model ($c_w = 2/3$) [57] (see [58] for a detailed discussion). Taking both into account, we consider an “effective” K-dominance zone which starts from where the stress peaks and ends at the location where the stress deviates from LEFM prediction, as shown in Fig. 4(c). Lastly, to calculate the LEFM prediction, we use the numerical stress intensity factor K_{IC}^{num} based on G_C^{num} shown in Eqn. 3.4.

Fig. 5 shows the result where we replace d/d_{max} with d/D_K . The transition can now be more quantitatively identified as $d = D_K$: the green region contains configurations satisfying $d > D_K$, and the orange region contains those satisfying $d < D_K$. $d = D_K$ also serves as a good location for the transition into crack deflection, i.e., when $d < D_K$. Although the inclusion size in configuration three is larger than D_K , the crack also shows a small degree of deflection, especially when compared to configurations one and two. This can be due to a combination of uncertainties associated with estimating D_K from the $(\sigma_{xx} + \sigma_{yy})/E_0 - r/a$ plot and inaccuracies associated with estimating D_K assuming a quasi-static fracture condition; the latter may not be very accurate when a crack crosses material heterogeneities due to nonnegligible crack speed effects [24, 25]. Nevertheless, our estimation of D_K is a good first-order approximation. We point out that d/D_K ranges from as small as ~ 0.4 to as large as ~ 3 . This range sits between the two extremes: zero and infinity. Suppose d is way smaller than D_K (approaching zero). In that case, we shall consider these inclusions as sub-meso scale heterogeneities whose contributions can be treated in a homogenized manner. As such, the crack tip effectively senses a homogeneous material field. If d is way larger than D_K (approaching infinity), we can consider these inclusions as layered heterogeneities that a crack can sense. However, there will not be crack deflections as the K-dominance zone is always encompassed by d (assuming negligible interfacial effects). Therefore, the mesoscale effects of inclusions only become pronounced when the inclusion size becomes comparable to that of the K-dominance zone. We emphasize again that the reported size effect emerges by assuming a strong connection (e.g., negligible interfacial effects) between the base medium and the inclusion. However, depending on the specific choice of materials, a (weak) interface can arise, leading to a crack deflecting along interfaces instead of into inclusions [47] regardless of the inclusion size. This kind of crack deflection can be more pronounced for interfaces with complex geometries [59], especially in a three-dimensional setting [60]. Incorporating interfacial effects is an exciting research direction we plan to investigate in the near future. Lastly, we note that this size interplay between inclusion and the K-dominance zone is reminiscent of that occurs at a smaller length scale [61]: the material heterogeneity becomes comparable to the size of the process zone, subsequently leading to a significant perturbation of the rupture dynamics.

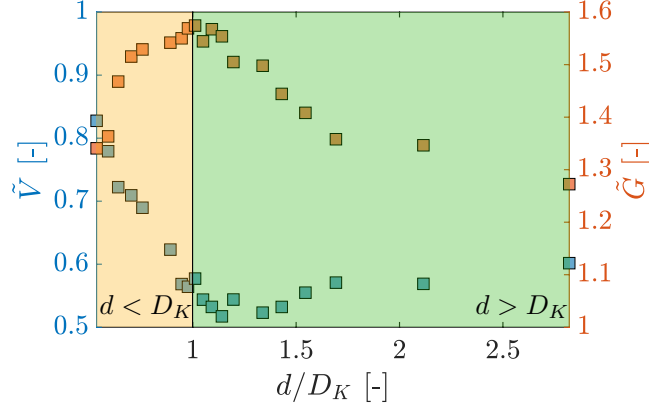


Figure 5: A similar plot to Fig. 3(a) but showing the variation of \tilde{V} and \tilde{G} as a function of normalized inclusion size d/D_K , with D_K identified from Fig. 4(c). It can be observed that D_K quantitatively identifies the transition from the green region ($d > D_K$) to the orange region ($d < D_K$).

We conclude by pointing out that the size of the K-dominance zone can thus be viewed as the minimum size for an inclusion to interact effectively with a crack. As a result, if given the same volume fraction of second-phase material, it is more efficient, in terms of toughening a material, to increase the number of inclusions that are available to interact effectively (so long as $d > D_K$) with a crack. Conversely, if given a varying volume fraction of second-phase material, is it possible to exploit the size interplay between d and D_K to achieve a better toughening outcome using a lower volume fraction configuration? From a design perspective, such a possibility can be helpful to achieve an optimal balance tradeoff between strength and toughness, especially for scenarios with limited choices of materials. We explore this possibility in the next section.

4.2. Applying to varying volume fraction with fixed inclusion material

We generate configurations with varied volume fraction $f_1 \propto N^{-1}$ with the resulting inclusion size d ranging from $\sim 0.06a$ to $\sim 0.3a$. Compared to configurations studied in the previous section, configurations here will have a smaller inclusion size d given the same N satisfying $N > 5$. Conversely, a similar-valued d corresponds to a configuration with fewer inclusions. We keep the inclusion material unchanged, so $\alpha = 0.4, \beta = 2.4$.

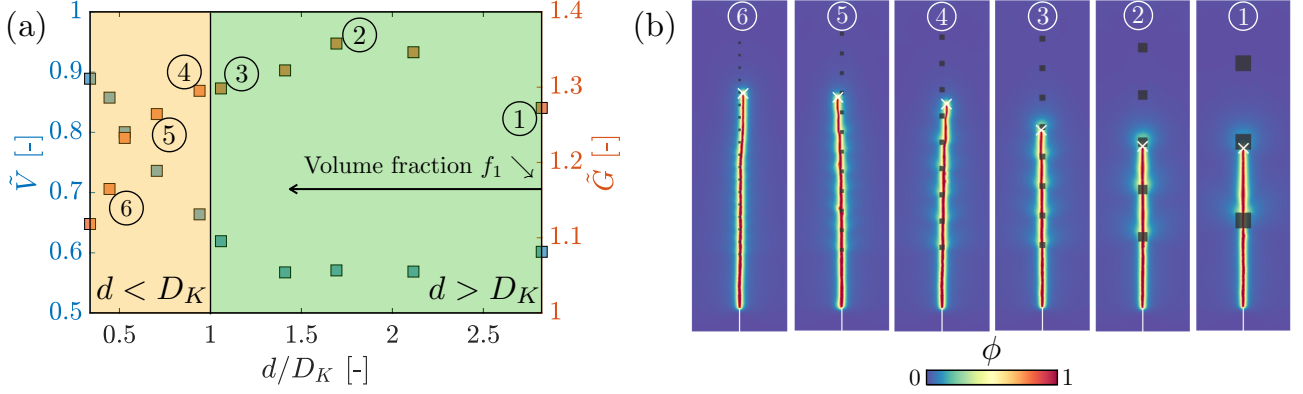


Figure 6: Scenarios with varying volume fractions. (a) Variation of \tilde{V} (blue square) and \tilde{G} (red square) as a function of d/D_K for configurations with different volume fractions $f_1 \propto N^{-1}$. (b) Visualizations of the final crack trajectory from the six configurations highlighted in (a) whose inclusion size and volume fraction increase from the left to the right.

Fig. 6(a) shows the variation of \tilde{V} (blue square) and of \tilde{G} (red square) as a function of d/D_K , with D_K taken directly from the previous section. Qualitatively, we can make two observations from this figure. First, a lower volume fraction of inclusion can indeed lead to a better toughening outcome, namely, lower (apparent) crack speed (\tilde{V}) and higher (apparent) fracture energy dissipation rate (\tilde{G}). Second, such a configuration occurs only when $d > D_K$; as d transitions into $d < D_K$, a lower volume fraction configuration always leads to a less effective toughening outcome (e.g., \tilde{G} becoming monotonically decreasing). As an example, configurations one and two have $d_1 > d_2$ but give $\tilde{V}_1 > \tilde{V}_2$ and $\tilde{G}_1 < \tilde{G}_2$; such a relation is nowhere to be found in the orange region where $d < D_K$. Here, $d = D_K$ does not lead to the best toughening outcome. For these configurations, decreasing inclusion size d simultaneously reduces the volume fraction (or the number of inclusion). As such, compared to configurations from the previous section, fewer inclusions are there to interact with a crack as we approach $d = D_K$ from the above. Fig. 6(b) shows the final crack trajectory for six configurations highlighted in Fig. 6(a). We can draw a similar observation by comparing to Fig. 3(b): when $d > D_K$ (configurations one, two, and three), the crack goes through inclusions; when $d < D_K$, the crack starts deflecting away. For configuration three, the crack begins to show a small degree of deflection even though the corresponding $d > D_K$. Again, this may be explained by approximations and uncertainties associated with estimating D_K . To conclude, configured appropriately, a lower volume fraction of inclusions can lead to a better toughening outcome if and only if the inclusion size approaches from above the size of the K-dominance zone. Results shown here also substantiate our argument that the size of the K-dominance zone can be viewed as the minimal size for an inclusion to interact effectively with a crack.

4.3. Extending to varying inclusion material with varying volume fraction

In this section, we extend our study to consider the effects of different inclusion materials (or different mechanical configurations of inclusions). We continue with the varying volume fraction setting, i.e., $f_1 \propto N^{-1}$. We consider three different kinds of materials using three different values for $\alpha\beta$: 0.45, 0.96, and 1.92, which lead to three different critical stress intensity factor values: $K_{IC, \text{in}} = \sqrt{0.45}K_{IC0}$, $K_{IC, \text{in}} = \sqrt{0.96}K_{IC0}$, and $K_{IC, \text{in}} = \sqrt{1.92}K_{IC0}$. Within each $K_{IC, \text{in}}$ value,

we consider three different combinations of α and β while keeping $\alpha\beta$ unchanged. For $\alpha\beta = 0.45$ we consider $\alpha = 0.2, \beta = 2.25$, $\alpha = 0.3, \beta = 0.5$, and $\alpha = 0.36, \beta = 1.25$. For $\alpha\beta = 0.96$ we consider $\alpha = 0.4, \beta = 2.4$ (already studied), $\alpha = 0.6, \beta = 1.6$, and $\alpha = 0.8, \beta = 1.2$. For $\alpha\beta = 1.92$ we consider $\alpha = 0.8, \beta = 2.4$, $\alpha = 1.0, \beta = 1.92$, and $\alpha = 1.2, \beta = 1.6$. Finally, we estimate two more D_K values in the same way described in the previous section using $E = E_0, G_C = 0.45G_{C0}$ and $E = E_0, G_C = 1.92G_{C0}$, respectively.

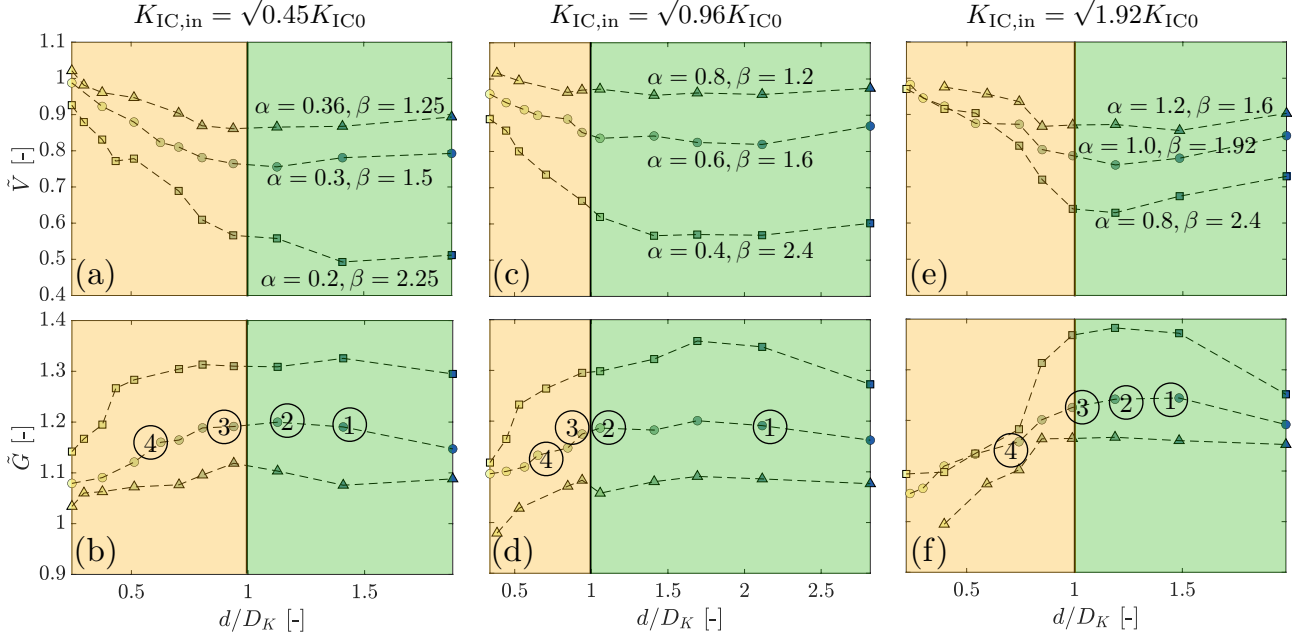


Figure 7: Variation of \tilde{V} (first row) and \tilde{G} (second row) as a function of d/D_K for different inclusion materials under the varying volume fraction setting $f_1 \propto N^{-1}$. Each column corresponds to an additional value of $\alpha\beta$: (a) and (b) in the first column corresponds to $\alpha\beta = 0.45$, (c) and (d) in the second column corresponds to $\alpha\beta = 0.96$, and (e) and (f) corresponds to $\alpha\beta = 1.92$. Each symbol (triangle, circle, and square) within each column of plots corresponds to a specific choice of α and β , whose values are shown within the plots in the first row.

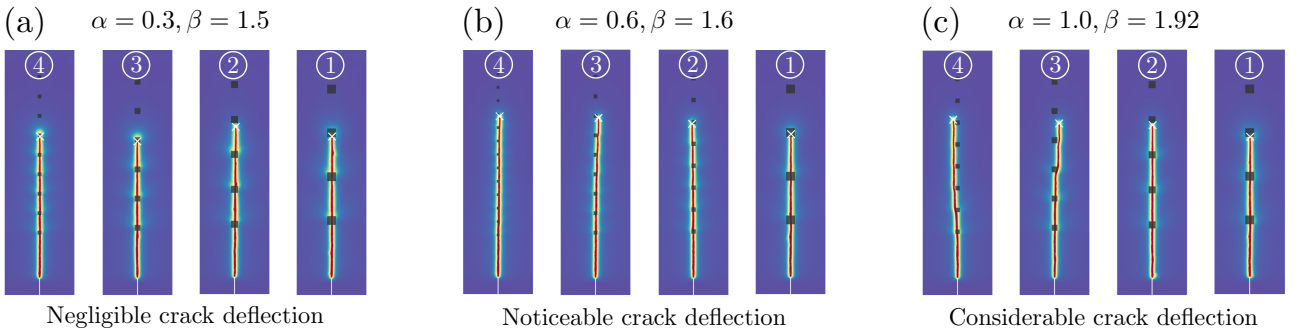


Figure 8: (a) Visualizations of the final crack trajectory for four different configurations highlighted in Fig. 7(b). (b) Similar visualizations to (a) but for configurations highlighted in Fig. 7(d). (c) Similar visualizations to (a) but for configurations highlighted in Fig. 7(f).

Fig. 7 shows the simulation results for different combinations of α and β , where the first row

corresponds to the variation of \tilde{V} as a function of d/D_K and the second row corresponds to that of \tilde{G} . Two conclusions can be drawn from this figure. First, changing the inclusion material will change D_K (thereby moving where d/D_K is) but will not remove the size interplay between the inclusion and the K-dominance zone. Indeed, in the green region where $d > D_K$, we can always find a configuration with a lower inclusion volume fraction that gives a better toughening outcome. On the contrary, in the orange region where $d < D_K$, a lower volume fraction always leads to a less effective toughening outcome. Second, the amount of toughening, in terms of the values of \tilde{V} and \tilde{G} , depends on the choice of α and β . In general, a more compliant (smaller α) and tougher (larger β) inclusion material will lead to a better toughening outcome, and this is well-documented [47]. We also note that the size interplay between d and D_K does not necessarily change the crack trajectory, as we have observed. Whether there is a change in the crack trajectory, and if so, the amount of change, also depends on the specific choice of inclusion material (values of α and β). Fig. 8 illustrates this point by showing the crack trajectories for three inclusion materials. Each subfigure corresponds to one inclusion material and contains four configurations highlighted in Fig. 7(b). In Fig. 8(a) where we use $\alpha = 0.3, \beta = 1.5$, there is no crack deflection as we cross the transition point $d/D_K = 1$ from configuration two to configuration three: the crack always goes through inclusions. In Fig. 8(b), where we change to $\alpha = 0.6, \beta = 1.6$, there is a noticeable amount of crack deflection as we cross $d/D_K = 1$. Lastly, in Fig. 8(c), where we change again to $\alpha = 1.0, \beta = 1.92$, we observe a more considerable amount of crack deflection as we cross $d/D_K = 1$.

5. Summary

Using a variational phase-field approach, we investigate mesoscale size effects of material heterogeneities on dynamic crack propagation in brittle solids under a quasi-static loading condition. We consider a simple case using a single array of square inclusions to represent mesoscale heterogeneities. We study how altering their geometrical (inclusion size and spacing) and mechanical (inclusion material) configurations can lead to different crack propagation patterns under a Mode-I loading condition. We summarize our main findings below:

- In the context of fracture, there is an interplay between the size of the inclusion and that of the K-dominance zone. Fixing the volume fraction of inclusions and matching the inclusion size d with the size of the K-dominance zone (D_K) leads to the best toughening outcome. Conversely, varying the volume fraction of inclusions, a lower volume fraction configuration can lead to a better toughening outcome if and only if those inclusions are configured appropriately with their size approaching from above the size of the K-dominance zone.
- The size of the K-dominance zone can therefore be viewed as the minimum size for an inclusion to interact effectively with a crack. Therefore, to toughen a piece of brittle solid, it is more efficient to increase the number of inclusions available to interact effectively with a crack (i.e., inclusion size being no smaller than that of the K-dominance zone).
- Changing the inclusion material can change the size of the K-dominance zone, the amount of toughening, and the crack trajectory (e.g., the amount of crack deflection). However, it does not remove the size interplay between the inclusion and the K-dominance zone.

Our work reveals the connection between the toughening effectiveness and the mesoscale size interplay between d and D_K , thereby opening a venue for the rational design of functional (meta-)materials that optimally balance the tradeoff between strength, stiffness, and toughness.

Looking ahead, we discuss several exciting research directions. The first one is extending to study the scenario where a crack can interact with multiple arrays of inclusions. In particular, when neighboring inclusions are close enough to induce stress modulations within the K-dominance zone, the crack trajectory may change and lead to a different toughening outcome. Experiments from [21] demonstrated that the toughening outcome under a single void array is quantitatively different from that under multiple void arrays and that void-void interactions play an important role in this regard. It will be interesting to check how translatable their observation is to our work, where inclusions are not voids but are made of different materials.

The second one is developing a more systematic and efficient approach to estimate D_K : Given an estimation of the application's and (mesoscale) defects' geometry and size, how do we quickly give a reliable estimation on the range of D_K considering crack evolution? Further, how significant is the effect of rapid crack motion on D_K ? Previous work has shown that increasing crack speed decreases the process zone size [61], which also implies a possible change to D_K . Does such a change of D_K require modifying the optimal design strategy obtained from a quasi-static estimation? In our work, the crack speed is not significant due to a quasi-static loading condition (partly due to our choices of inclusion materials). Therefore, estimating D_K using a quasi-static approximation seems accurate enough from a design perspective. However, the crack speed can fluctuate significantly for dynamic loading conditions and even approach the Rayleigh wave speed when interacting with heterogeneities [26]. In these scenarios, a quasi-static approximation may not hold, and a dynamic formula considering the effect of instantaneous crack tip speed is needed [24, 62]. Moreover, early experiments have suggested the possible lack of the K-dominance zone due to the highly transient nature of the crack tip motion [63, 64] under dynamic loadings, whose implication toward our finding merits further investigation. Studying the variation of D_K as a function of different loading rates (as well as crack speed) can therefore be helpful for applications in extreme conditions such as high-speed impact.

The third one is studying the potential implication of our findings to inclusions taking the form of voids. In these cases, we may consider voids as spacings and the materials in between as inclusions. Using the same void size, a recent study [23] showed that a smaller volume fraction of voids (i.e., a more significant volume fraction of inclusions) leads to a better toughening outcome, which is qualitatively consistent with our findings. It will be, however, interesting to study more systematically and quantitatively the size interplay between void, spacing, and the K-dominance zone associated with the base material.

The last one is considering interfacial effects [47], which are not included in our current numerical model but can become significant depending on the choice of material and inclusion size and shape [59], especially in a three-dimensional setting [60].

6. CRediT Authorship Contribution Statement

L Li. Conceptualization, Methodology, Software, Formal Analysis, Investigation, Writing – Original & Draft, Visualization. **J Rao.** Methodology – Crack tip tracking algorithm, Writing – Appendix B. **TC Hufnagel.** Resources, Supervision, Writing – Review & Editing,

Funding acquisition, Project Administration. **KT Ramesh**. Conceptualization, Resources, Supervision, Writing – Review & Editing, Funding Acquisition, Project Administration.

7. Acknowledgements

The authors gratefully acknowledge the financial support provided by the Corning Research and Development Corporation, and for stimulating discussions on glass ceramics with Dr. Jason Harris, Dr. Charlene Smith, and Dr. Xinyi Xu from Corning.

Appendix A. Implementation and verification of our phase-field simulator

Following [40] for modeling fracture in brittle solids, we decompose the elastic strain energy shown in Eqn. 2.1 to a tensile part (“+”) and a compressive part (“−”), with the phase-field acting only on the former:

$$\mathcal{W}^e(\epsilon_{ij}, \phi) = [(1 - k)(1 - \phi)^2 + k]\mathcal{W}^{e,+}(\epsilon_{ij}) + \mathcal{W}^{e,-}(\epsilon_{ij}), \quad (\text{A.1})$$

where $\epsilon_{ij} = (u_{i,j} + u_{j,i})/2$ is the infinitesimal strain tensor, and k is a user-defined small constant used for numerical convenience, preventing $\mathcal{W}^{e,+}$ from vanishing as $\phi \rightarrow 1$. To compute $\mathcal{W}^{e,+}$ and $\mathcal{W}^{e,-}$, we first calculate the tensile part ϵ^+ and the compressive part ϵ^- of ϵ using spectral decomposition [40]:

$$\epsilon_{ij} = \epsilon_{ij}^+ + \epsilon_{ij}^-, \quad (\text{A.2})$$

$$\text{with } \epsilon_{ij}^+ = \sum_{d=1}^2 \langle \epsilon^d \rangle_+ n_i^d n_j^d, \quad (\text{A.3})$$

$$\text{and } \epsilon_{ij}^- = \sum_{d=1}^2 \langle \epsilon^d \rangle_- n_i^d n_j^d, \quad (\text{A.4})$$

where ϵ^d is the d -th eigenvalue of ϵ , n^d is the corresponding eigenvector, $\langle x \rangle_+$ stands for $(x + |x|)/2$, and $\langle x \rangle_-$ stands for $(x - |x|)/2$ with $|x|$ being the absolute value of x . We can then express $\mathcal{W}^{e,+}(\epsilon_{ij})$ and $\mathcal{W}^{e,-}(\epsilon_{ij})$ as the following:

$$\mathcal{W}^{e,+}(\epsilon_{ij}) = \frac{1}{2} \lambda \langle \epsilon_{kk} \rangle_+^2 + \mu \epsilon_{kj}^+ \epsilon_{jl}^+ \delta_{kl}, \quad (\text{A.5})$$

$$\mathcal{W}^{e,-}(\epsilon_{ij}) = \frac{1}{2} \lambda \langle \epsilon_{kk} \rangle_-^2 + \mu \epsilon_{kj}^- \epsilon_{jl}^- \delta_{kl}, \quad (\text{A.6})$$

where λ and μ are the Lamé constants that can be determined from the Young’s modulus E and the Poisson’s ratio ν . Applying the principle of least action to Eqn. 2.1 with \mathcal{W}^e expressed using Eqns. A.1, A.5 and A.6, we arrive at the following two governing equations:

$$\sigma_{ij,j} + b_i = \rho \ddot{u}_i, \quad (\text{A.7})$$

$$\left[1 + \frac{4c_w \ell (1 - k)}{G_C} \mathcal{W}^{e,+} \right] \phi - \ell^2 \phi_{,ii} = \frac{4c_w \ell (1 - k)}{G_C} \mathcal{W}^{e,+}, \quad (\text{A.8})$$

where $\sigma_{ij} = \partial \mathcal{W}^e / \partial \epsilon_{ij}$. We enforce the irreversible growth condition $\dot{\phi} > 0$ using a strain-history field [40] over the simulation domain:

$$\mathcal{H}(x, t) = \max_{s \in [0, t]} \mathcal{W}^{e,+}(\epsilon(x, s)) \quad \forall x \in \Omega. \quad (\text{A.9})$$

Replacing $\mathcal{W}^{e,+}$ with $\mathcal{H}(x, t)$ in Eqn. A.8 we then want to solve:

$$\sigma_{ij,j} + b_i = \rho \ddot{u}_i, \quad (\text{A.10})$$

$$\left[1 + \frac{4c_w \ell (1 - k)}{G_C} \mathcal{H} \right] \phi - \ell^2 \phi_{,ii} = \frac{4c_w \ell (1 - k)}{G_C} \mathcal{H}, \quad (\text{A.11})$$

together with the following Neumann boundary conditions (plus any existing Dirichlet boundary conditions) :

$$\sigma_{ij} n_j = t_i \text{ on } \partial\Omega, \quad (\text{A.12})$$

$$\phi_{,i} n_i = 0 \text{ on } \partial\Omega. \quad (\text{A.13})$$

We solve Eqns. A.10 and A.11 weakly based on a standard finite element discretization and calculation procedure, using the alternating minimization (or staggered) scheme. We verify our implementation using published simulation results of the classical Kalthoff-Winkler experiment [50]. Fig. A.9(a) shows the simulation domain and boundary condition, where we also take advantage of the symmetric nature of the experiment to reduce computational cost. We model the impactor by applying the following velocity to the lower left boundary:

$$v = \begin{cases} \frac{t}{t_0} v_0 & t \leq t_0, \\ v_0 & t > t_0, \end{cases} \quad (\text{A.14})$$

with $v_0 = 16.5$ m/s and $t_0 = 1$ μ s. The material properties are taken from [28]: $\rho = 8000$ kg/m³, $E = 190$ GPa, $\nu = 0.3$, and $G_C = 2.213 \times 10^4$ J/m². We use $k = 1 \times 10^{-12}$ as the small constant used for preventing $\mathcal{W}^{e,+}$ from vanishing. We model the initial crack as an explicit discontinuity that resembles a sharp wedge. We use $\ell = 3.9 \times 10^{-4}$ m and $t = 0.04$ μ s. We refine elements around where the crack is expected to propagate and ensure the element size within the refined region $\delta < \ell/2$. Figs. A.9(b) and A.9(c) show the temporal evolution of the total elastic energy and dissipated energy obtained from our simulator, respectively. Our results agree well with those extracted from [28] considering multiple element sizes. Fig. A.10 shows the temporal evolution of crack trajectory for four different time instants, all of which agree qualitatively with measurements from experiments [50] and simulations [28].

Appendix B. Introduction to our crack tip tracking algorithm

We identify the boundary of a crack using a user-defined phase field value ϕ_c . We pick $\phi_c = 0.85$ in this work. This algorithm finds what can be considered the tip of the boundary (i.e., the crack tip) in four steps (see Fig. B.11): starting from the phase field and mesh data at a particular time step, it first reconstructs the iso-curve, isolates points near the tip, resamples these points, then computes the tip by looking for symmetries in the curvature. The algorithm is efficient and parallelizable, as multiple time steps can be analyzed simultaneously.

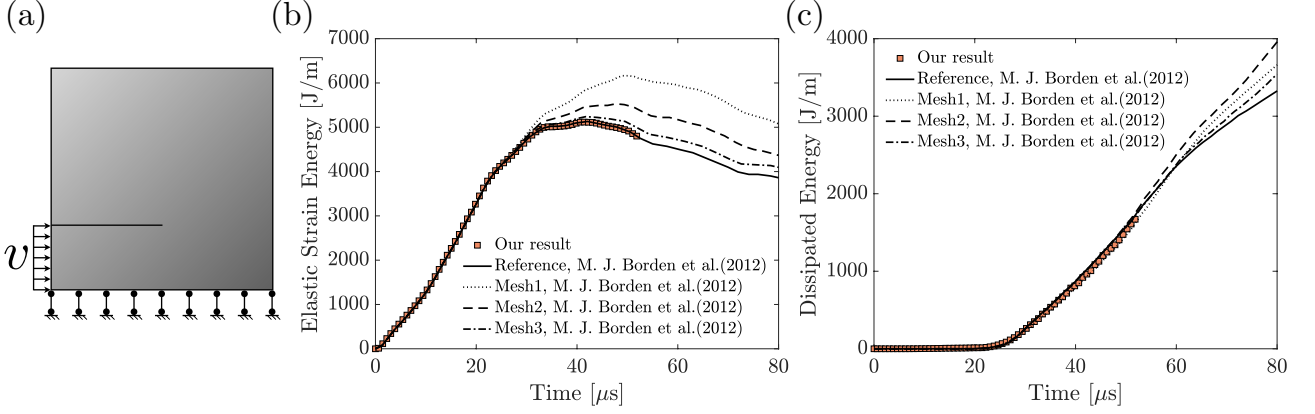


Figure A.9: (a) Geometry and boundary condition of the simulation domain. (b) Temporal evolution of the system's kinetic energy obtained from our simulator (red circle) and from [28] using various element sizes (curves colored in black). (c) A plot similar to (b) shows the temporal evolution of the system's dissipated energy through fracture.

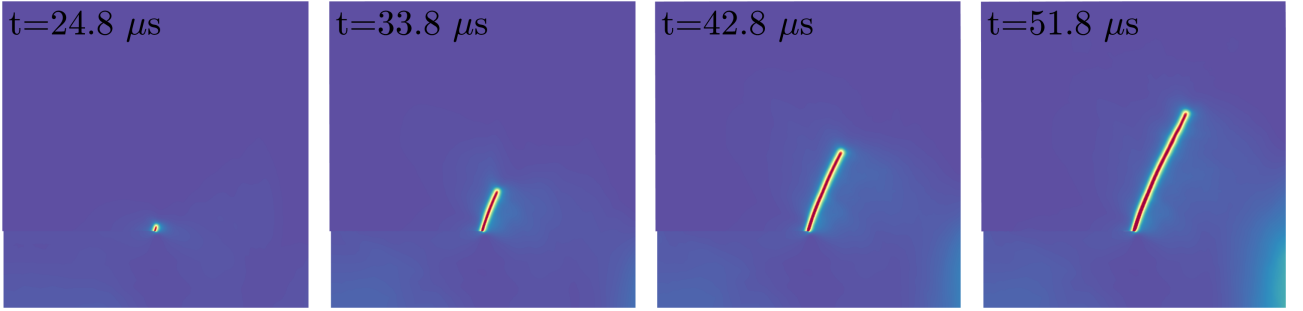


Figure A.10: Snapshots obtained from our simulation showing the crack trajectory at four different time instants: $t = 24.8 \mu\text{s}$, $t = 33.8 \mu\text{s}$, $t = 42.8 \mu\text{s}$, and $t = 51.8 \mu\text{s}$.

The algorithm first constructs the iso-curve from the phase field and mesh data of a given time step. Here, the iso-curve is represented by a list of ordered pairs, $[(x_1, y_1), (x_2, y_2), \dots, (x_n, y_n)]$, where each ordered pair represents a point in which the isocurve intersects with an element edge. The algorithm computes this list by looping through all elements and stopping when encountering an element (denoted as $\#n$) whose nodal phase field values $\phi_{n1}, \phi_{n2}, \phi_{n3}$ satisfy $\phi_{ni} < \phi_c < \phi_{nj}$ for at least one edge of that element. Then, starting from the edge (n_i, n_j) , it uses knowledge of mesh connectivity to look for the next edge where $\phi_{ni} < \phi_c < \phi_{nj}$. It stores the (x, y) location of where $\phi = \phi_c$ on an edge (n_i, n_j) as the next element in the list $[(x_1, y_1), (x_2, y_2), \dots, (x_n, y_n)]$. The algorithm terminates when no more adjacent edges $\phi_{ni} < \phi_c < \phi_{nj}$ can be found. It then travels in reverse to sample the rest of the iso-curve.

From the list $[(x_1, y_1), (x_2, y_2), \dots, (x_n, y_n)]$, the algorithm moves to isolate points on the iso-curve that are near the approximate location of the tip. This step is necessary because the end goal is to obtain the tip location using symmetries in the curvature of the iso-curve. However, this method can easily misidentify the tip in particularly straight cracks (which have a uniform curvature of zero along the sides) or cracks with even curvature throughout. Thus, points of $\phi = \phi_c$ near the crack tip are first found and isolated. This is done by finding the closest vector between two points within some user-defined anti-parallel threshold. Specifically,

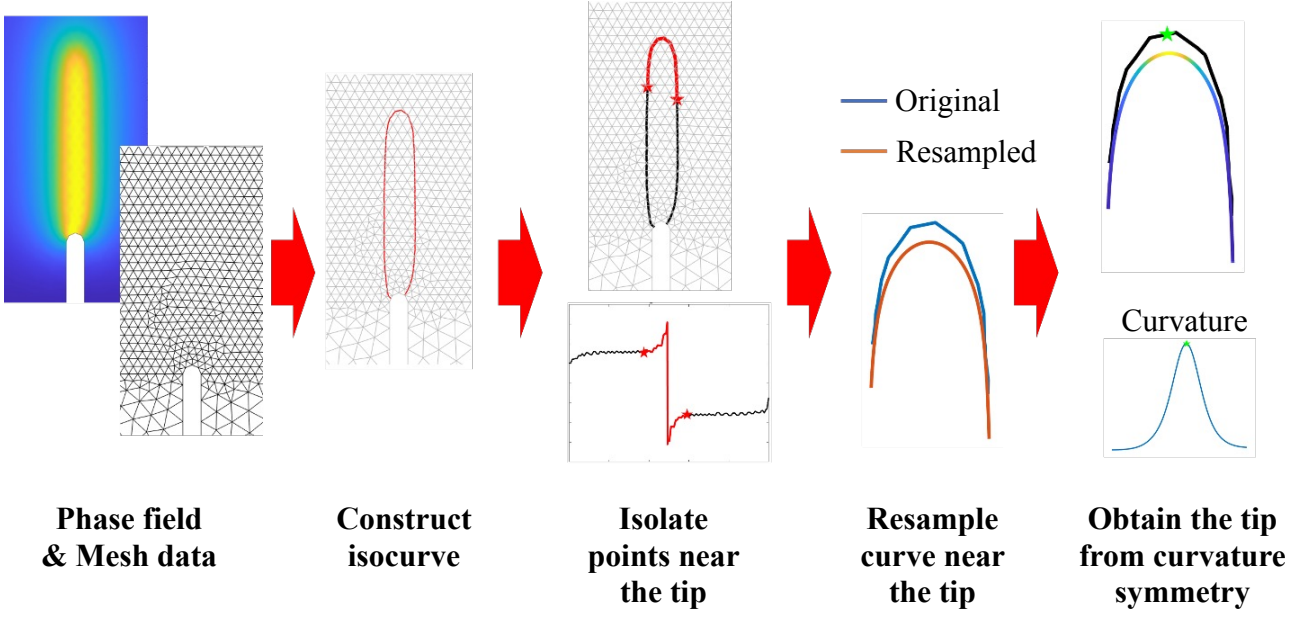


Figure B.11: A schematic demonstrating our crack tip tracking method.

let $\mathbf{x}_1 = (x_i, y_i)$, $\mathbf{x}_2 = (x_j, y_j)$ be two points on the iso-curve where $i < j$. We wish to find the combination of (i, j) such that the quantity $j - i$ is as small as possible, and that $\frac{\mathbf{x}_1 \cdot \mathbf{x}_2}{|\mathbf{x}_1||\mathbf{x}_2|} \approx -1$. In practice, we simply stop the algorithm when $\frac{\mathbf{x}_1 \cdot \mathbf{x}_2}{|\mathbf{x}_1||\mathbf{x}_2|}$ is within some range centered at -1 . Following this step, an approximate envelope consisting of the tip can be identified by a new list containing a reduced number of points $[(x_i, y_i), (x_{i+1}, y_{i+1}), \dots, (x_{j-1}, y_{j-1}), (x_j, y_j)]$. From this new list, the points are resampled with a greater density using linear interpolation and a Gaussian smoothing process (to remove discontinuities in the curvature). Denoting the resampled curve to be $[(x_1^R, y_1^R), \dots, (x_{n_R}^R, y_{n_R}^R)]$, where n_R is the total number of points created in the resampling process. Then, a simple curvature calculation is performed on this curve using numerical differentiation. More specifically, since the points of the iso-curve are in an ordered list, the curvature κ at any point i can be found by

$$\kappa_i = \frac{[(x_{i+1} - x_{i-1})^2 + (y_{i+1} - y_{i-1})^2]^{3/2}}{|(x_{i+1} - x_{i-1})(y_{i+2} - 2y_i + y_{i-2}) - (x_{i+2} - 2x_i + x_{i-2})(y_{i+1} - y_{i-1})|}, \quad (\text{B.1})$$

which is essentially the numerical formulation of the curvature of a pair of parameterized functions in Cartesian coordinates:

$$\kappa = \frac{[(x')^2 + (y')^2]^{3/2}}{|x'y'' - x''y'|}. \quad (\text{B.2})$$

This calculation results in a list of curvatures $(\kappa_3, \kappa_4, \dots, \kappa_{n_R-2})$, and the algorithm proceeds to look for the point κ_i where the curvature plot is most symmetrical within some window l . This is done by summing the quantity $(\kappa_{i-k} - \kappa_{i+k})^2$ where $k = 1, 2, \dots, l$. Essentially, we compute the difference between a point with an indicial distance k on the left-hand side of i and a point

with an indicial distance k on the right-hand side of i . We square this difference, and we sum this value over all possible values of k from 1 to l . This means computing:

$$\text{Error associated with point } i = \sum_{k=1}^l (\kappa_{i-k} - \kappa_{i+k})^2. \quad (\text{B.3})$$

The lower this error, the more symmetrical the curve is around the point i . Since we need to use a window of size l to calculate this error, we do not consider points within an indicial distance of l from the end of the resampled curve to avoid issues with this calculation. Then, the point with the lowest error is denoted as the crack tip for the considered time step. The actual location of the tip is found by the identical index $i + 2$ in the non-smoothed version of the resampled curve. We add this 2 because the curvature calculation removed two entries from the indices.

References

- [1] Robert O Ritchie. The conflicts between strength and toughness. *Nature materials*, 10(11):817–822, 2011.
- [2] MZ Hossain, C-J Hsueh, B Bourdin, and K Bhattacharya. Effective toughness of heterogeneous media. *Journal of the Mechanics and Physics of Solids*, 71:15–32, 2014.
- [3] Michael F Ashby and Kara Johnson. *Materials and design: the art and science of material selection in product design*. Butterworth-Heinemann, 2013.
- [4] FC Serbena, I Mathias, CE Foerster, and ED Zanolto. Crystallization toughening of a model glass-ceramic. *Acta Materialia*, 86:216–228, 2015.
- [5] GC Wei and PF Becher. Improvements in mechanical properties in sic by the addition of tic particles. *Journal of the American Ceramic Society*, 67(8):571–574, 1984.
- [6] Xiaoyu Zheng, Howon Lee, Todd H Weisgraber, Maxim Shusteff, Joshua DeOtte, Eric B Duoss, Joshua D Kuntz, Monika M Biener, Qi Ge, Julie A Jackson, et al. Ultralight, ultrastiff mechanical metamaterials. *Science*, 344(6190):1373–1377, 2014.
- [7] Lucas R Meza, Satyajit Das, and Julia R Greer. Strong, lightweight, and recoverable three-dimensional ceramic nanolattices. *Science*, 345(6202):1322–1326, 2014.
- [8] Tobias Frenzel, Muamer Kadic, and Martin Wegener. Three-dimensional mechanical metamaterials with a twist. *Science*, 358(6366):1072–1074, 2017.
- [9] Yifan Wang, Liuchi Li, Douglas Hofmann, José E Andrade, and Chiara Daraio. Structured fabrics with tunable mechanical properties. *Nature*, 596(7871):238–243, 2021.
- [10] Tian Chen, Mark Pauly, and Pedro M Reis. A reprogrammable mechanical metamaterial with stable memory. *Nature*, 589(7842):386–390, 2021.

- [11] Ke Liu, Rachel Sun, and Chiara Daraio. Growth rules for irregular architected materials with programmable properties. *Science*, 377(6609):975–981, 2022.
- [12] Muamer Kadic, Graeme W Milton, Martin van Hecke, and Martin Wegener. 3d metamaterials. *Nature Reviews Physics*, 1(3):198–210, 2019.
- [13] Xiaoxing Xia, Christopher M Spadaccini, and Julia R Greer. Responsive materials architected in space and time. *Nature Reviews Materials*, 7(9):683–701, 2022.
- [14] Angkur Jyoti Dipanka Shaikhee, Huachen Cui, Mark O’Masta, Xiaoyu Rayne Zheng, and Vikram Sudhir Deshpande. The toughness of mechanical metamaterials. *Nature materials*, 21(3):297–304, 2022.
- [15] Daicong Da, Yu-Chin Chan, Liwei Wang, and Wei Chen. Data-driven and topological design of structural metamaterials for fracture resistance. *Extreme Mechanics Letters*, 50:101528, 2022.
- [16] Yingqi Jia, Oscar Lopez-Pamies, and Xiaojia Shelly Zhang. Controlling the fracture response of structures via topology optimization: From delaying fracture nucleation to maximizing toughness. *Journal of the Mechanics and Physics of Solids*, 173:105227, 2023.
- [17] Konstantinos Karapiperis and Dennis M Kochmann. Prediction and control of fracture paths in disordered architected materials using graph neural networks. *Communications Engineering*, 2(1):32, 2023.
- [18] Tommaso Magrini, Chelsea Fox, Adeline Wihardja, Athena Kolli, and Chiara Daraio. Control of mechanical and fracture properties in two-phase materials reinforced by continuous, irregular networks. *arXiv preprint arXiv:2309.01888*, 2023.
- [19] Simon Heide-Jørgensen, Michal K Budzik, and Kevin T Turner. Mechanics and fracture of structured pillar interfaces. *Journal of the Mechanics and Physics of Solids*, 137:103825, 2020.
- [20] Sage Fulco, Michal K Budzik, Erich D Bain, and Kevin T Turner. Decoupling toughness and strength through architected plasticity. *Extreme Mechanics Letters*, 57:101912, 2022.
- [21] Yu Liu, L St-Pierre, NA Fleck, VS Deshpande, and A Srivastava. High fracture toughness micro-architected materials. *Journal of the Mechanics and Physics of Solids*, 143:104060, 2020.
- [22] Kaitlynn M Conway, Cody Kunka, Benjamin C White, Garrett J Pataky, and Brad L Boyce. Increasing fracture toughness via architected porosity. *Materials & Design*, 205:109696, 2021.
- [23] NR Brodnik, Stella Brach, CM Long, G Ravichandran, B Bourdin, KT Faber, and K Bhattacharya. Fracture diodes: Directional asymmetry of fracture toughness. *Physical Review Letters*, 126(2):025503, 2021.
- [24] Lambert Ben Freund. *Dynamic fracture mechanics*. Cambridge university press, 1998.

- [25] Gabriele Albertini, Mathias Lebihain, François Hild, Laurent Ponson, and David S Kammer. Effective toughness of heterogeneous materials with rate-dependent fracture energy. *Physical Review Letters*, 127(3):035501, 2021.
- [26] Giuliano Lazzaroni, Renaud Bargellini, Pierre-Emmanuel Dumouchel, and Jean-Jacques Marigo. On the role of kinetic energy during unstable propagation in a heterogeneous peeling test. *International Journal of Fracture*, 175:127–150, 2012.
- [27] Jean-Claude Michel and Pierre Suquet. Merits and limits of a variational definition of the effective toughness of heterogeneous materials. *Journal of the Mechanics and Physics of Solids*, 164:104889, 2022.
- [28] Michael J Borden, Clemens V Verhoosel, Michael A Scott, Thomas JR Hughes, and Chad M Landis. A phase-field description of dynamic brittle fracture. *Computer Methods in Applied Mechanics and Engineering*, 217:77–95, 2012.
- [29] Neal R Brodnik, Chun-Jen Hsueh, Katherine T Faber, Blaise Bourdin, Guruswami Ravichandran, and Kaushik Bhattacharya. Guiding and trapping cracks with compliant inclusions for enhancing toughness of brittle composite materials. *Journal of Applied Mechanics*, 87(3):031018, 2020.
- [30] John W Cahn and John E Hilliard. Free energy of a nonuniform system. i. interfacial free energy. *The Journal of chemical physics*, 28(2):258–267, 1958.
- [31] John Lowengrub and Lev Truskinovsky. Quasi-incompressible cahn–hilliard fluids and topological transitions. *Proceedings of the Royal Society of London. Series A: Mathematical, Physical and Engineering Sciences*, 454(1978):2617–2654, 1998.
- [32] Xiaojing Fu, Luis Cueto-Felgueroso, and Ruben Juanes. Nonequilibrium thermodynamics of hydrate growth on a gas-liquid interface. *Physical Review Letters*, 120(14):144501, 2018.
- [33] Sara Najem and Martin Grant. Phase-field model for collective cell migration. *Physical Review E*, 93(5):052405, 2016.
- [34] Siavash Monfared, Guruswami Ravichandran, José Andrade, and Amin Doostmohammadi. Mechanical basis and topological routes to cell elimination. *Elife*, 12:e82435, 2023.
- [35] Blaise Bourdin, Gilles A Francfort, and Jean-Jacques Marigo. Numerical experiments in revisited brittle fracture. *Journal of the Mechanics and Physics of Solids*, 48(4):797–826, 2000.
- [36] Blaise Bourdin, Gilles A Francfort, and Jean-Jacques Marigo. The variational approach to fracture. *Journal of elasticity*, 91:5–148, 2008.
- [37] Andrew Akerson. Optimal structures for failure resistance under impact. *Journal of the Mechanics and Physics of Solids*, 172:105172, 2023.

- [38] Erwan Tanné, Tianyi Li, Blaise Bourdin, J-J Marigo, and Corrado Maurini. Crack nucleation in variational phase-field models of brittle fracture. *Journal of the Mechanics and Physics of Solids*, 110:80–99, 2018.
- [39] Michael Janssen, Jan Zuidema, and Russell Wanhill. *Fracture mechanics: fundamentals and applications*. CRC Press, 2004.
- [40] Christian Miehe, Martina Hofacker, and Fabian Welschinger. A phase field model for rate-independent crack propagation: Robust algorithmic implementation based on operator splits. *Computer Methods in Applied Mechanics and Engineering*, 199(45-48):2765–2778, 2010.
- [41] Alan Arnold Griffith. Vi. the phenomena of rupture and flow in solids. *Philosophical transactions of the royal society of london. Series A, containing papers of a mathematical or physical character*, 221(582-593):163–198, 1921.
- [42] Tymofiy Gerasimov and Laura De Lorenzis. Second-order phase-field formulations for anisotropic brittle fracture. *Computer Methods in Applied Mechanics and Engineering*, 389:114403, 2022.
- [43] Fatemeh Amiri, Daniel Millán, Marino Arroyo, Mohammad Silani, and Timon Rabczuk. Fourth order phase-field model for local max-ent approximants applied to crack propagation. *Computer Methods in Applied Mechanics and Engineering*, 312:254–275, 2016.
- [44] Marreddy Ambati, Tymofiy Gerasimov, and Laura De Lorenzis. Phase-field modeling of ductile fracture. *Computational Mechanics*, 55:1017–1040, 2015.
- [45] Jinhyun Choo and WaiChing Sun. Coupled phase-field and plasticity modeling of geological materials: From brittle fracture to ductile flow. *Computer Methods in Applied Mechanics and Engineering*, 330:1–32, 2018.
- [46] Stella Brach, Erwan Tanné, Blaise Bourdin, and Kaushik Bhattacharya. Phase-field study of crack nucleation and propagation in elastic–perfectly plastic bodies. *Computer Methods in Applied Mechanics and Engineering*, 353:44–65, 2019.
- [47] He Ming-Yuan and John W Hutchinson. Crack deflection at an interface between dissimilar elastic materials. *International journal of solids and structures*, 25(9):1053–1067, 1989.
- [48] Shahed Rezaei, Jaber Rezaei Mianroodi, Tim Brepols, and Stefanie Reese. Direction-dependent fracture in solids: Atomistically calibrated phase-field and cohesive zone model. *Journal of the Mechanics and Physics of Solids*, 147:104253, 2021.
- [49] Liuchi Li, Konstantinos Karapiperis, and José E Andrade. Emerging contact force heterogeneity in ordered soft granular media. *Mechanics of Materials*, 162:104055, 2021.
- [50] Joerg F Kalthoff. Modes of dynamic shear failure in solids. *International Journal of fracture*, 101(1-2):1–31, 2000.

- [51] Luigi Ambrosio and Vincenzo Maria Tortorelli. Approximation of functional depending on jumps by elliptic functional via t -convergence. *Communications on Pure and Applied Mathematics*, 43(8):999–1036, 1990.
- [52] JD Achenbach and LM Brock. On quasistatic and dynamic fracture. In *Proceedings of an international conference on Dynamic Crack Propagation*, pages 529–541. Springer, 1973.
- [53] Michael Smith. Abaqus/standard user’s manual, version 6.9. 2009.
- [54] Christian Miehe, Fabian Welschinger, and Martina Hofacker. Thermodynamically consistent phase-field models of fracture: Variational principles and multi-field fe implementations. *International journal for numerical methods in engineering*, 83(10):1273–1311, 2010.
- [55] Max L Williams. On the stress distribution at the base of a stationary crack. 1957.
- [56] TL Becker Jr, JM McNaney, RM Cannon, and RO Ritchie. Limitations on the use of the mixed-mode delaminating beam test specimen: Effects of the size of the region of k -dominance. *Mechanics of Materials*, 25(4):291–308, 1997.
- [57] Kim Pham, Hanen Amor, Jean-Jacques Marigo, and Corrado Maurini. Gradient damage models and their use to approximate brittle fracture. *International Journal of Damage Mechanics*, 20(4):618–652, 2011.
- [58] Philip K Kristensen, Christian F Niordson, and Emilio Martínez-Pañeda. An assessment of phase field fracture: crack initiation and growth. *Philosophical Transactions of the Royal Society A*, 379(2203):20210021, 2021.
- [59] MT Aranda, IG García, A Quintanas-Corominas, and J Reinoso. Crack impinging on a curved weak interface: Penetration or deflection? *Journal of the Mechanics and Physics of Solids*, page 105326, 2023.
- [60] Mathias Lebihain, Jean-Baptiste Leblond, and Laurent Ponson. Effective toughness of periodic heterogeneous materials: the effect of out-of-plane excursions of cracks. *Journal of the Mechanics and Physics of Solids*, 137:103876, 2020.
- [61] Fabian Barras, Philippe H Geubelle, and Jean-François Molinari. Interplay between process zone and material heterogeneities for dynamic cracks. *Physical review letters*, 119(14):144101, 2017.
- [62] K Ravi-Chandar. *An experimental investigation into the mechanics of dynamic fracture*. PhD thesis, California Institute of Technology, 1982.
- [63] K Ravi Chandar and WG Knauss. Dynamic crack-tip stresses under stress wave loading—a comparison of theory and experiment. *International Journal of Fracture*, 20:209–222, 1982.
- [64] Hareesh V Tippur, Sridhar Krishnaswamy, and Ares J Rosakis. Optical mapping of crack tip deformations using the methods of transmission and reflection coherent gradient sensing: a study of crack tip k -dominance. *International Journal of Fracture*, 52:91–117, 1991.